Measuring and Simulating the Local Packing Density Resulting From Ultrasound-Directed Self-Assembly of Spherical Microparticles into Specific Patterns

Soheyl Noparast[1], Fernando Guevara Vasquez[2], Mathieu Francoeur[3,4] and Bart Raeymaekers[1,*]

[1]*Department of Mechanical Engineering, Virginia Tech, Blacksburg, Virginia 24061, USA*
[2]*Department of Mathematics, University of Utah, Salt Lake City, Utah 84112, USA*
[3]*Department of Mechanical Engineering, University of Utah, Salt Lake City, Utah 84112, USA*
[4]*Department of Mechanical Engineering, McGill University, Montréal, Quebec H3A 0C3, Canada*

Ultrasound-directed self-assembly (DSA) enables organizing and orienting particles dispersed in a fluid medium into specific patterns, thus agglomerating them into pattern features with different packing density than when first dispersed in the fluid medium. In this paper, we theoretically derive and experimentally validate a three-dimensional model of the ultrasound DSA process to simulate and quantify the local packing density of spherical microparticles when assembled into pattern features. We study the packing density as a function of process parameters, including particle volume fraction, particle size, and medium viscosity. The results show that the local particle packing density increases with increasing particle volume fraction and reaches a maximum of 45% independent of medium viscosity. Also, the local particle packing density increases with decreasing particle size for constant particle volume fraction. The results shed light on the relationship between the process parameters and the local particle packing density within pattern features resulting from ultrasound DSA. This knowledge is useful in the context of using ultrasound DSA to manufacture engineered composite materials that require high particle packing density, or packing density gradients, e.g., to increase mechanical or electrical properties, or to tailor combustion of energetic particles, among other applications.

I. INTRODUCTION

Ultrasound-directed self-assembly (DSA) relies on the acoustic radiation force associated with a standing ultrasound wave to organize and orient spherical or high-aspect-ratio particles dispersed in a fluid medium into specific patterns [1,2]. Theoretical work to study the acoustic radiation force began in the 1930s with King [3], who considered incompressible spherical particles suspended in an inviscid fluid. Yosioka and Kawasima [4] extended King's analysis to compressible spherical particles in an inviscid fluid. In 1962, Gor'kov [5] generalized these results in an acoustic radiation force theory for compressible spherical particles, smaller than the acoustic wavelength, and dispersed in an inviscid fluid. Recently, Settnes and Bruus [6] extended Gor'kov's theory to include fluid viscosity; they showed that the acoustic radiation force in a viscous fluid compared to an inviscid fluid changes by multiple orders of magnitude. Additionally, Noparast *et al.* [7] theoretically derived and experimentally demonstrated that the location where particles assemble during ultrasound DSA depends

on the fluid viscosity and particle volume fraction, because the sound-propagation velocity of the mixture of fluid and particles is a function of the viscosity and particle volume fraction.

The acoustic radiation force results from scattering, and drives particles to the locations where the acoustic radiation force approaches zero, and the time-averaged acoustic radiation potential is locally minimum, which coincides with the nodes or antinodes of the standing ultrasound wave, depending on the compressibility of the particles and the fluid medium, respectively [1,2]. Thus, the particle packing density is higher where particles assemble than outside of those locations, or compared to when particles are randomly dispersed in the fluid medium. When particles are closely packed, a secondary acoustic radiation force results from their interaction. Bjerknes [8] studied this interaction force between a pair of bubbles in an acoustic field, followed by others who studied the interaction force between a pair of incompressible particles in an inviscid [9–11] and viscous [12] fluid, respectively. Silva and Bruus [13] theoretically derived the interaction force between a pair of compressible particles in an inviscid fluid and subject to a plane acoustic wave, considering

---

*bart.raeymaekers@vt.edu

monopole and dipole single scattering. Zhang *et al.* [14] studied the interaction forces between multiple spherical particles assembled at the (anti)node of a standing acoustic wave. They derived an analytical expression that accounts for multiple monopole and dipole scattering, but solved it for single scattering only due to the computational cost of multiple scattering simulations.

In contrast to other external field DSA methods, such as electric [15,16] or magnetic [17,18] fields, which pose strict requirements on the material properties of the particle, the existence of the acoustic radiation force is only dependent on the acoustic contrast between the particles and the medium, which derives from their density and compressibility [19]. Additionally, low attenuation of ultrasound waves in low-viscosity media enables scalability of ultrasound DSA, especially in comparison to electric and magnetic fields [20]. Hence, ultrasound DSA finds application in a myriad of engineering applications, such as noncontact particle manipulation [21,22], manipulation of cells in biological experiments [23,24], and biomedical devices [25,26]. Furthermore, integrating ultrasound DSA with different manufacturing methods, including freeze casting [27,28] and mold casting [29–31], enables fabricating engineered polymer composite materials with user-specified organization and orientation of the filler within the matrix. This, in turn, allows tailoring the properties of the composite material, including structural [30–32], electrical [33–35], thermal [36], energetic [37–39], or multifunctional properties [40]. Furthermore, integrating ultrasound DSA with additive manufacturing (AM) [33,40–49], including vat polymerization (VP) [40,46–49] and direct ink writing (DIW) [42–44], enables manufacturing engineered polymer matrix composite materials in a layer-by-layer fashion, where in each layer ultrasound DSA organizes and orients filler into specific patterns and orientations.

In this paper, we quantify the local particle packing density within the pattern features that result from ultrasound DSA, as a function of particle volume fraction, particle size, and medium viscosity. This knowledge is particularly helpful when using ultrasound DSA to manufacture materials where high particle packing density is required, e.g., to increase mechanical [31] or electrical [34] properties, or to tailor the combustion of energetic particles [37,39,50], among other applications.

The literature defines the particle packing density as the volume fraction of a control volume occupied by solid material [51]. Theoretical work documents the maximum packing density of spherical particles in different configurations, including bcc = 0.68 and fcc = 0.74 [52]. Additionally, the maximum packing density of randomly organized spherical particles is between 0.55–0.63 [53–55]. Others document that the particle packing density increases with particle volume fraction [51], independent of particle size [55]. Additionally, the literature documents

comparisons between experiments and theoretical results of particle packing density measurements [56,57]. Mixing two (binary distribution) and three (ternary distribution) particle sizes increases the packing density compared to that of a single particle size, because small particles fit into cavities between large particles [58]. Furthermore, for a binary distribution, the particle packing density increases with increasing particle size ratio but also depends on the particle volume fraction of small and large particle sizes [55,58–60].

Specifically related to particle packing density resulting from ultrasound DSA, Niendorf and Raeymaekers [48] determined the microscale and macroscale alignment of microfibers using ultrasound DSA as a function of particle volume fraction. They concluded that microscale and macroscale microfiber alignment decrease and increase, respectively, with increasing volume fraction as a result of increasing microscale entanglement and increasing number of fibers. Additionally, Greenhall *et al.* [31] documented that the mechanical properties of engineered polymer matrix composite materials increase with increasing volume fraction of carbon nanotubes, and they quantified the local particle volume fraction after ultrasound DSA. Similarly, Scholz *et al.* [41] reported increasing mechanical properties with increasing volume fraction of glass fibers. Thus, changing the local packing density of particles allows tuning the properties of the engineered polymer matrix composite material.

No other work relates the ultrasound DSA process parameters to the local particle packing density within the pattern features that result from ultrasound DSA, despite its relevance in manufacturing engineered polymer matrix composite materials with tailored properties. Thus, the objective of this paper is to theoretically derive and experimentally validate a three-dimensional (3D) model to simulate, quantify, and predict the local packing density of spherical particles at the pattern features that result from ultrasound DSA. We quantify the 3D particle packing density using numerical simulations of the ultrasound DSA process. Additionally, we experimentally measure the local particle packing density within the pattern features that result from ultrasound DSA, fixated in place using a vat polymerization setup.

II. METHODS AND MATERIALS

A. Theoretical model and simulation

We simulate the 3D assembly of spherical particles dispersed in a viscous medium contained in a reservoir, during the ultrasound DSA process, as a function of particle volume fraction, particle size, and medium viscosity. Figure 1(a) schematically illustrates a spherical particle in a viscous medium exposed to an ultrasound wave field, showing the forces acting on the particle, in addition to the local normalized acoustic pressure and the acoustic
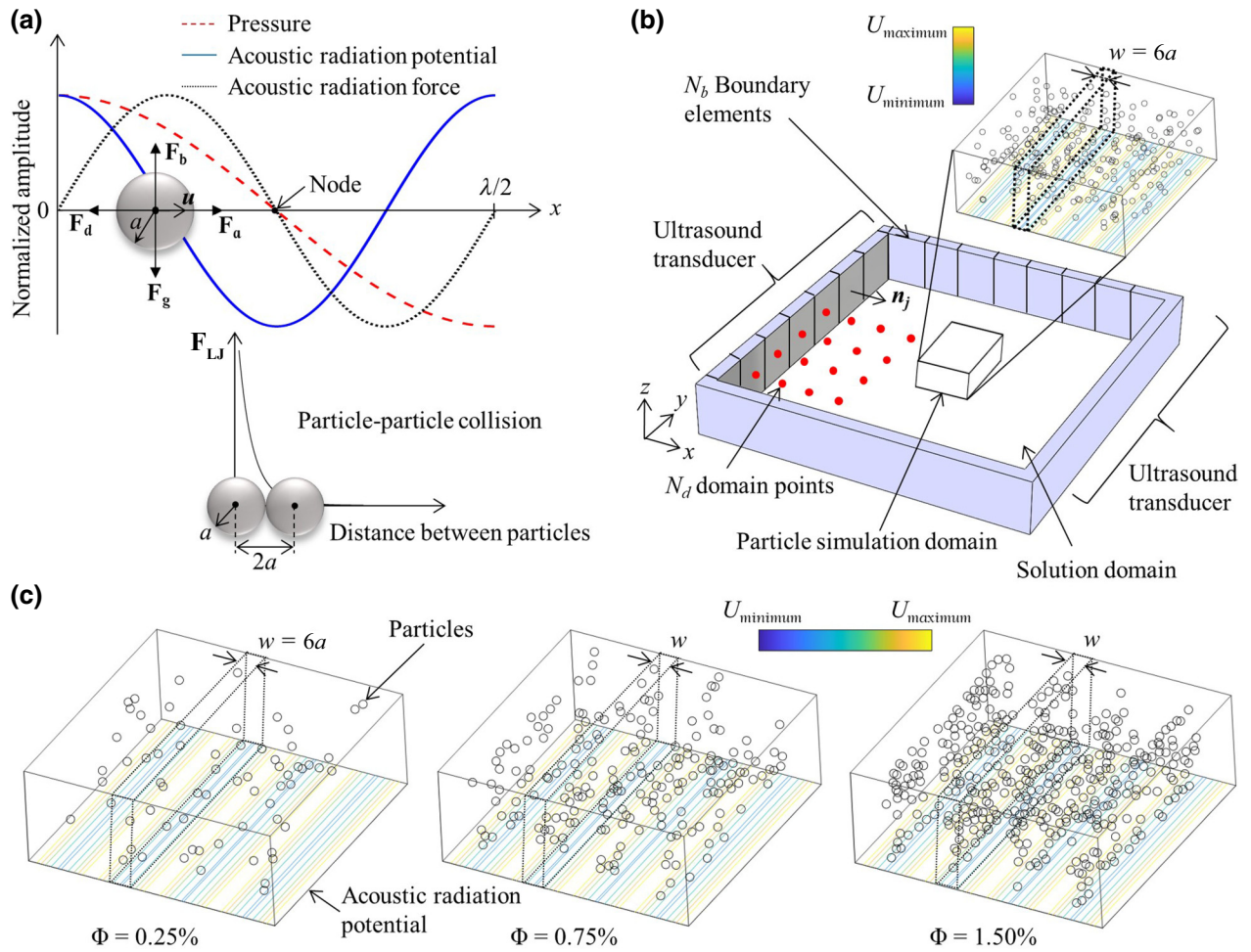
FIG. 1. (a) Schematic of a spherical particle in a viscous medium, and in a standing ultrasound wave field during ultrasound DSA, indicating the different forces acting on the particle. (b) Schematic of the 3D theoretical model of the reservoir with two ultrasound transducers affixed to opposing walls that contains the mixture of spherical particles dispersed in the viscous medium, showing the solution domain within a simply closed boundary. (c) Simulated 3D particle location for different particle volume fractions.

radiation potential. A particle with radius a experiences the acoustic radiation force $\mathbf{F_a}$ that drives it to the local minimum of the time-averaged acoustic radiation potential, in addition to the Stokes' drag force with Oseen's correction $\mathbf{F_d}$ that resists the motion of the particle in the viscous medium. Also, each particle experiences both gravity $\mathbf{F_g}$ and buoyancy forces $\mathbf{F_b}$, which depend on the mass of the particle and the density of the viscous medium, respectively. In our model, when particles collide with each other or the wall of the reservoir that contains the mixture of particles and viscous medium, we use a truncated Lennard-Jones-like potential to create a repulsive force $\mathbf{F_{LJ}}$ that accounts for the collisions. Figure 1(b) schematically shows a reservoir with two ultrasound transducers affixed to opposing walls, which contains a mixture of spherical particles dispersed in a viscous medium. Energizing the ultrasound transducers establishes a standing ultrasound wave in the reservoir,

which we simulate at the N_d domain points in the 3D solution domain that covers the entire reservoir [red dots in Fig. 1(b)] using the boundary element method (BEM) based on the Helmholtz equation $\nabla^2\varphi_{\text{inc}} + \tilde{k}^2\varphi_{\text{inc}} = 0$. Here, $\tilde{k} = (\omega/c_m)/(1 - i\omega\tau_s)^{1/2}$ is the complex wave number that accounts for acoustic attenuation in a viscous medium [20] and φ_{inc} is the incident velocity potential. $\omega = 2\pi f$ and f are the angular and temporal frequency of the ultrasound wave field, c_m is the sound propagation velocity within the viscous medium, $\tau_s = 4\eta_m/3\rho_m c_m^2$ is the relaxation time (i.e., viscous dissipation time to dampen the acoustic pressure to $1/e$ of its original value), with η_m and ρ_m the viscosity and density of the viscous medium, and $i = (-1)^{1/2}$ [20].

We represent the reservoir as a simply closed boundary with N_b boundary elements that enclose the 3D solution domain with N_d domain points. A boundary element j represents either a part of the reservoir wall with velocity

$v_j = 0$, or a part of an ultrasound transducer that acts as a piston source with velocity $v_j = v_0 e^{i(\omega t - \theta)}$ along its normal direction $\mathbf{n}_j$, with v_0 the real velocity amplitude and ω and θ the angular frequency and phase of the ultrasound wave, respectively. We impose the impedance boundary condition $\partial \varphi_{\text{inc}} / \partial \mathbf{n}_j + ik\widetilde{Z}\varphi_{\text{inc}} = v_j$ at each boundary element, with $k = \omega/c_m = 2\pi/\lambda$ and λ is the wavelength of the standing ultrasound wave. $\widetilde{Z} = Z_m/Z_b$ accounts for the absorption and reflection of the ultrasound wave at the boundary of the reservoir; we maintain the acoustic impedance Z_b constant along the entire boundary, and the acoustic impedance of the medium is $Z_m = \rho_m c_m$.

We simulate the 3D motion of N nonoverlapping particles, randomly dispersed in the fluid medium as a function of time, resulting from the forces acting on the particles [see Fig. 1(a)]. The N particles are located in the particle simulation domain, which is the center section of the solution domain [see Fig. 1(b)], because it is too computationally expensive to track particles in the entire solution domain. We calculate the velocity potential φ that results from single scattering of all spherical particles in the 3D particle simulation domain, and we assume they behave like monopole and dipole scatterers, with $ka \ll 1$. $k = Re\{\tilde{k}\} = 2\pi/\lambda$ is the wave number and λ is the wavelength of the standing ultrasound wave. The velocity potential at location $\mathbf{r}_i$ of the ith particle is given as [13]

$$\varphi(\mathbf{r}_i) = \varphi_{\text{inc}}(\mathbf{r}_i) + \sum_{\substack{j=1 \\ j \neq i}}^{N} \varphi_{\text{sc}}(\mathbf{r}_i | \mathbf{r}_j), \qquad (1)$$

which is the superposition of the incident velocity potential φ_{inc} at $\mathbf{r}_i$ calculated using the BEM method, and the sum of velocity potentials resulting from single scattering off all N particles j at $\mathbf{r}_j$. The scattered velocity potential from the jth particle at the location of the ith particle $\mathbf{r}_i$ is [13]

$$\varphi_{\text{sc}}(\mathbf{r}_i | \mathbf{r}_j) = -i(ka)^3 \left[\frac{f_1}{3} h_0^{(1)}(k||\mathbf{r}_i - \mathbf{r}_j||)\varphi_{\text{inc}}(\mathbf{r}_j) \right. $$
$$\left. - \frac{f_2}{2} h_1^{(1)}(k||\mathbf{r}_i - \mathbf{r}_j||) \frac{\partial \varphi_{\text{inc}}(\mathbf{r}_j)}{\partial (k||\mathbf{r}_i - \mathbf{r}_j||)} \right] \quad (2)$$

with $f_1 = 1 - \beta_p/\beta_m$ and $f_2 = Re\{[2(1 - \gamma)(\rho_p/\rho_m - 1)]/[2\rho_p/\rho_m + 1 - 3\gamma]\}$. Here, $\gamma = -3/2[1 + i(1 + \delta/a)]\delta/a$, with $\delta = (2\eta_m/\omega\rho_m)^{1/2}$ the viscous boundary layer thickness around a particle [6]. $\beta_p = 1/[\rho_p(c_{p,c}^2 - 4c_{p,s}^2/3)]$, ρ_p, $\beta_m = 1/(\rho_m c_m^2)$, and ρ_m are the compressibility and the density of the spherical particle and medium, respectively [19]. $c_{p,c}$ and $c_{p,s}$ represent the compressional and shear wave propagation velocities. $h_0^{(1)}(z) = -ie^{iz}/z$ and $h_1^{(1)}(z) = -e^{iz}(z+i)/z^2$ are zeroth- and first-order spherical Hankel functions of the first kind [61]. $||\mathbf{r}_i - \mathbf{r}_j||$ is the Euclidean distance between locations $\mathbf{r}_i$ and $\mathbf{r}_j$,

and $\partial \varphi_{\text{inc}}(\mathbf{r}_j)/\partial ||\mathbf{r}_i - \mathbf{r}_j||$ is the derivative of the incident velocity potential at location $\mathbf{r}_j$ in the direction of $\mathbf{r}_i - \mathbf{r}_j$. We emphasize that in our model, the particle simulation domain is several wavelengths removed from the boundaries of the solution domain and, thus, we assume that the interaction between the scattered wave field and the boundary elements is negligible. Note that the monopole scattering coefficient f_1 involves the compressibility contrast of the particles and the medium, whereas the dipole scattering coefficient f_2 involves the mass density contrast and it also accounts for the effect of medium viscosity on dipole scattering. Doinikov [62] also emphasized that the thermal effects can cause imperfect behavior of the medium surrounding the particle in a standing ultrasound wave, which affects the monopole scattering coefficient f_1 when the depth of penetration of the thermal wave $\delta_t = [2\kappa_m/(\rho_m c_{p,m}\omega)]^{1/2}$ is comparable to the particle radius a. κ_m and $c_{p,m}$ are the thermal conductivity and specific heat of the medium, respectively. For the range of parameters in this work $0.005 \leq \delta_t/a \leq 0.02$ and, thus, we neglect the thermal effects in our 3D simulation model.

The ultrasound wave velocity $\mathbf{v} = \nabla\varphi$ and the pressure $p = i\rho_m \omega\varphi$. Hence, the time-averaged acoustic radiation potential U in the viscous medium is [6]

$$U = \frac{4\pi}{3} a^3 \left(f_1 \frac{\beta_m}{2} \langle p^2 \rangle - f_2 \frac{3\rho_m}{4} \langle v^2 \rangle \right). \qquad (3)$$

Operators $\langle \cdot \rangle$ and $Re\{\cdot\}$ represent the time average over a wave period and the real part of the expression, respectively. The acoustic radiation force $\mathbf{F_a} = -\nabla U$. Thus, we first calculate the incident velocity potential φ_{inc} in all domain points of the solution domain using a complex wave number in the Helmholtz equation to account for the acoustic wave attenuation. Second, we calculate the velocity potential φ in all domain points of the particle simulation domain as the summation of the incident velocity potential φ_{inc} and single monopole and dipole scattering from other particles in the simulation domain. Finally, we calculate the acoustic radiation potential and force on all particles in the particle simulation domain.

Additionally, the Stokes drag force with Oseen's correction that acts on each particle is $\mathbf{F_d} = 12\pi a^2 \rho_m ||\mathbf{u}||^2(1 + 3/16\text{Re})/\text{Re}$, which orients in the same direction and opposite sense of the particle velocity $\mathbf{u}$. $\text{Re} = 2a\rho_m||\mathbf{u}||/\eta_m$ is the Reynolds number [63]. Furthermore, we account for particle-particle and particle-wall collisions using the repulsive portion of a Lennard-Jones-like potential $V_{\text{LJ}} = 4\varepsilon_{\text{LJ}}(2a/r)^{12}$. The force acting on two particles within a distance r of each other is $\mathbf{F_{LJ}} = -\nabla V_{\text{LJ}}$ [64]. We tune ε_{LJ} following an iterative procedure in which we average the smallest distance between neighboring particles over a finite time until the average minimum distance

between colliding particles equals $2a$ ($\pm 2\%$) and between particles and a wall equals a ($\pm 2\%$).

We simulate the ultrasound DSA process over a duration $0 \leq t \leq T$ with time step Δt. When $t = 0$, the particles are stationary $||\mathbf{u}|| = 0$ and dispersed at randomly chosen, nonoverlapping locations in the 3D particle simulation domain. When $t > 0$, $||\mathbf{u}|| \neq 0$ because the sum of all forces acting on the particle [see Fig. 1(a)] accelerates the particle towards a local minimum of the time-averaged acoustic radiation potential, where the particles assemble. In each time step Δt, we calculate the location and velocity of each particle $\mathbf{u}$ after accounting for particle-particle collisions.

Finally, when all particles have assembled at $t = T$, we determine the 3D particle packing density as the volume of particles within a cuboid of width w around the local minimum of the time-averaged acoustic radiation potential (node of the standing ultrasound wave) divided by the volume of the cuboid. Figure 1(c) illustrates this concept, showing a cuboid of width w (dashed line) around the node of the standing ultrasound wave, highlighting the particles that are partially or fully enclosed by it. The color map shows the time-averaged acoustic radiation potential in arbitrary units. We determine w based on the experiments (see Sec. II B).

We define three nondimensional parameters based on dimensional analysis using the Buckingham π theorem, which characterizes the local particle packing density at the pattern features that result from ultrasound DSA. We consider the following parameters in the simulations: the particle volume fraction $0 \leq \Phi \leq 27.5\%$ to show the maximum reachable local packing density, the nondimensional particle size $0.05 \leq K_1 = ka \leq 0.20$ to not violate the Rayleigh regime assumption ($ka \ll 1$), and the nondimensional viscosity of the medium $3.3 \times 10^3 \leq K_2 = \rho_m \lambda c_m / \eta_m \leq 9.8 \times 10^3$. The range of K_2 derives from the medium viscosity $150 \leq \eta_m \leq 450$ mPa s to span the viscosity of commercial photopolymer resins.

B. Experimental setup and parameter study

Figure 2(a) schematically shows the experimental setup we use to manufacture material specimens for a full-factorial study of the local particle packing density as a function of Φ and K_1. Parameter K_2 does not affect the steady-state local packing density after ultrasound DSA; it determines only the speed by which particles assemble, which we do not consider in this work. The setup is based on a VP digital light processing (DLP) printer (mUVe 1.1 DLP, Grand Rapids, Michigan, USA), augmented with an acrylic, square reservoir with two ultrasound transducers (piezoelectric ceramic plate, center frequency $f_c = 1.5$ MHz, Steminc, Florida, USA) affixed to opposing walls, to perform ultrasound DSA of particles

dispersed in the photopolymer resin. A function generator (Tektronix AFG 3102, Beaverton, Oregon, USA) and rf power amplifier (E&I 2100L, Rochester, New York, USA) energize the ultrasound transducers. The operating frequency f of the ultrasound wave field is close to the center frequency f_c of the ultrasound transducers. We use standard photopolymer resin (3DRS standard V2 gray resin, $c_m = 1420$ m/s, $\rho_m = 1100$ kg/m^3, $\eta_m = 218$ mPa s, 3D Resin Solutions, Illinois, USA) and spherical aluminum microparticles ($a = 15$ μm and 22 μm, $c_{p,c} = 6420$ m/s, $c_{p,s} = 3040$ m/s, $\rho_p = 2710$ kg/m^3 [65], US5005 solid aluminum spherical powder, US Research Nanomaterials, Inc., Texas, USA). Based on these materials, the values of nondimensional parameters are $0 \leq \Phi \leq 1.50\%$, $K_1 = 0.1$ and 0.15, and $K_2 = 6.8 \times 10^3$. The ranges of parameter values are driven by the feasibility of the experiments and relevance to manufacturing of engineered polymer matrix composite materials. Increasing the particle volume fraction increases acoustic wave attenuation, which decreases the magnitude of the acoustic radiation force and, thus, the ability to assemble particles at the nodes of the standing ultrasound wave. Furthermore, it increases the viscosity of the mixture of particles and medium, which requires increasing the acoustic radiation force to overcome the drag force exerted on the particles. Finally, it also increases the curing time required to fabricate a composite material specimen in the VP setup, which potentially leads to distortion of the pattern features. Thus, we choose particle sizes ($a = 15$ and 22 μm) that satisfy the Rayleigh regime assumption ($ka = 0.10$ and $0.15 \ll 1$) and are observable under an optical microscope. In addition, increasing the particle size increases their mass, which could cause them to precipitate to the bottom of the reservoir prior to assembly into pattern features. The choice of the medium viscosity ($\eta_m = 218$ mPa s) results from the availability of commercial photopolymer resins.

We disperse a volume fraction Φ of particles in the photopolymer resin using sonication to minimize particle aggregation (80 W, 2 min, UP200Ht, Hielscher, Teltow, Germany), after which we energize the ultrasound transducers for $T = 10$ s. The acoustic radiation force drives the particles to the nodes of the standing ultrasound wave, where they assemble and agglomerate. We fixate them in place by curing a 12×12 mm specimen using the DLP light source in the VP printer for 8 s. We postcure the specimen outside the DLP printer for 120 s, to eliminate any liquid resin. Figure 2(a) shows a typical material specimen after curing ($\Phi = 1.00\%$, $K_1 = 0.10$).

We experimentally measure the local particle packing density as the volume of particles within a cuboid of width w around the location where particles assemble (node of the standing ultrasound wave) divided by the volume of the cuboid, as a function of the nondimensional parameters Φ and K_1. The measurement is based on the notion that particle area fraction (the fraction of a surface covered
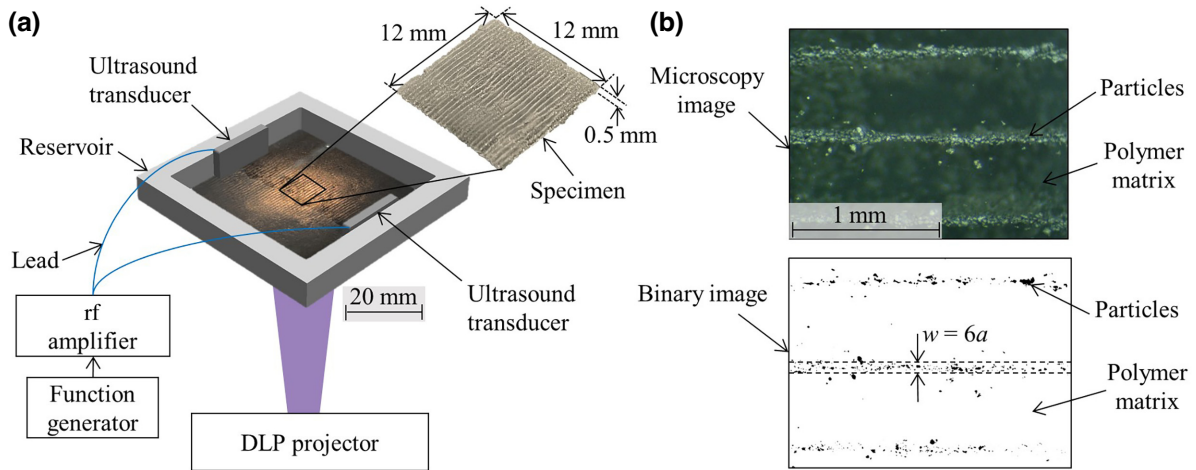
FIG. 2. (a) Schematic of the experimental setup, showing the VP DLP printer augmented with ultrasound DSA, and illustrating a typical material specimen that consists of photopolymer and aluminum particles. (b) Schematic of the measurement methodology, showing an optical micrograph with the corresponding binary image, and indicating the domain $w = 6a$ over which we determine the particle packing density.

by particles) is a good approximation to the 3D particle packing density, as originally documented by Underwood [66], and verified for accuracy using our 3D simulation model (maximum 4% error at $\Phi = 1.5\%$). Thus, the particle area fraction within a rectangle of width w around where particles assemble represents the particle packing density within a cuboid of width w around where particles assemble. Figure 2(b) schematically illustrates the measurement. We obtain optical micrographs (1.5 μm spatial resolution, $180\times$ magnification, AmScope, California, USA) of locations where we qualitatively observe good organization of the microparticles at the nodes of the standing ultrasound wave. The photopolymer matrix appears dark and the aluminum microparticles appear bright colored in a typical optical microscopy image [see Fig. 2(b)]. To accurately determine the surface area covered by aluminum particles, we binarize the image using a threshold that equates the particle area fraction of the entire image to the particle volume fraction Φ used to manufacture the material specimens [see Fig. 2(b)]. Thus, we focus the optical microscope on the top surface of the specimen and ensure to consider only particles on the surface of the specimen and not in the bulk, while simultaneously controlling for external influences, such as lighting conditions and glare. For each microscopy image, we determine the particle area fraction and, thus, the particle packing density, within a domain $w = Na$ centered around a node of the standing ultrasound wave, and we compare the experimental and simulation results [see Fig. 2(b)]. We select $N = 6$, i.e., $w = 6a$ to encompass most particles that assemble at the node of a standing ultrasound wave, based on experiments with $\Phi = 1.00\%$. We repeat each measurement 3 times for different material specimens and report the average, minimum, and maximum.

III. RESULTS AND DISCUSSION

Figure 3 shows the results of the full-factorial parameter study of the local particle packing density as a function of ultrasound DSA operating parameters. Figure 3(a) shows the local particle packing density at the location where particles assemble (node of the standing ultrasound wave) as a function of the particle volume fraction Φ and the nondimensional particle size K_1. We show the particle packing density obtained from simulations PD_{sim} (hollow markers) and experiments PD_{exp} (solid markers) for $K_1 = 0.10$ (black dot) and $K_1 = 0.15$ (blue square). The solid markers represent the average of three experiments, whereas the error bars show the minimum and maximum values. Furthermore, we label the data points in Fig. 3(a) and provide the corresponding optical microscopy images and binary images (white = resin, black = particles) in Fig. 3(b) to illustrate the results. Figure 3(c) shows magnified binary images.

From Fig. 3 we observe that the particle packing density increases with increasing volume fraction Φ and with decreasing K_1, as expected. Increasing Φ increases the number of particles at the node of the standing ultrasound wave because when $\Phi < 1.5\%$, the maximum local packing density is less than 10% [see Fig. 3(a)], which is much smaller than the maximum theoretical packing density for spherical particles of approximately 60% [53]. Furthermore, decreasing $K_1 = ka$ either requires reducing k, which increases λ and, thus, increases the number of particles that assemble at a node of the standing ultrasound wave (for constant Φ). Alternatively, it requires reducing a, which increases the number of particles for constant Φ, thus increasing the particle packing density at a node of the standing ultrasound wave. Also, we observe from
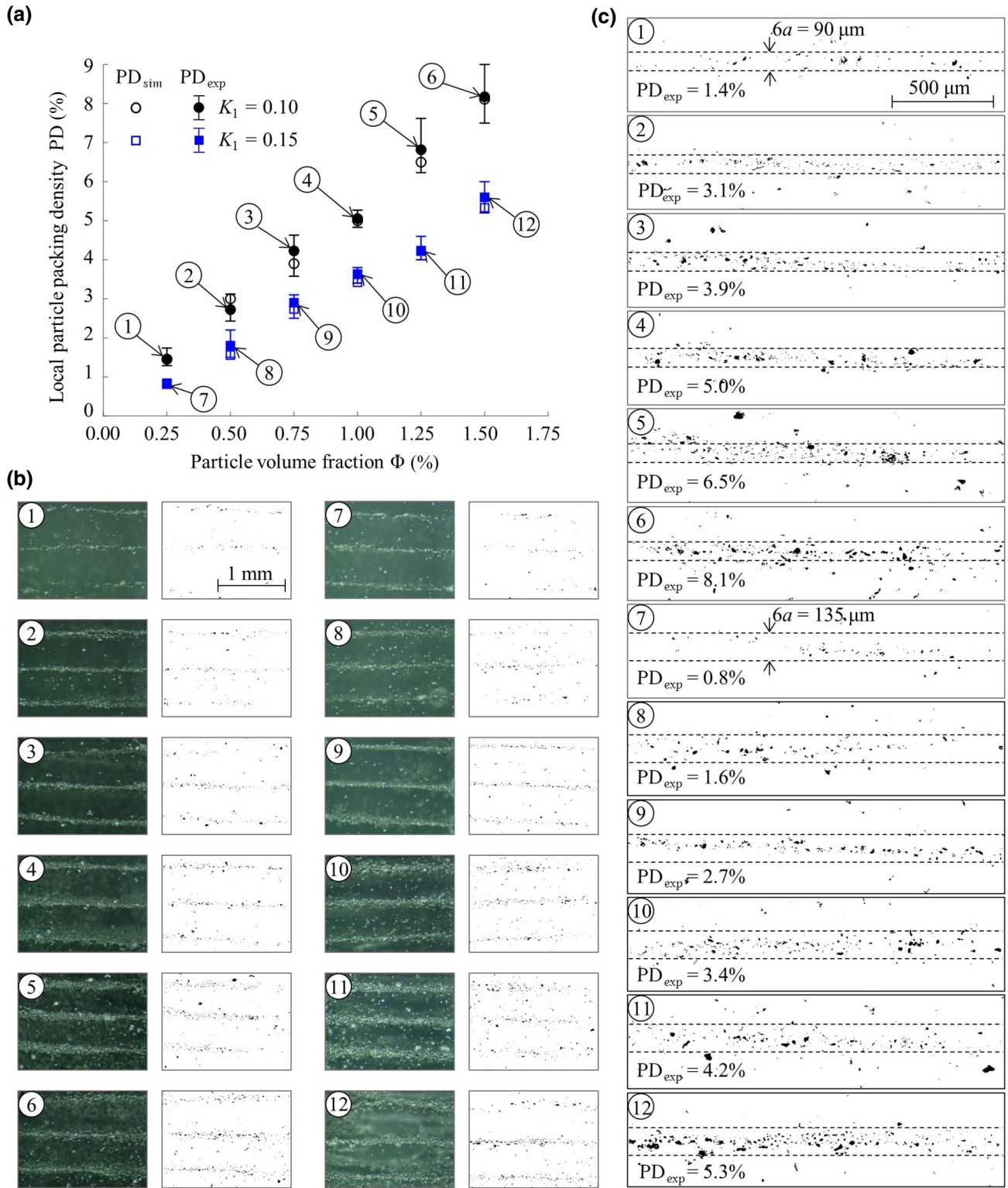
FIG. 3. (a) Local packing density within the pattern features that result from ultrasound DSA (node of the standing ultrasound wave) as a function of the particle volume fraction Φ, showing simulation PD_{sim} (hollow markers) and experiment PD_{exp} (solid markers) results for $K_1 = 0.10$ (black dot) and $K_1 = 0.15$ (blue square). (b) Optical microscopy images and binary images (white = resin, black = particles) for the data points in (a). (c) Magnified binary images that show the particles (black) and the domain over which we quantify PD_{exp}.

Fig. 3 that the theoretical simulations and experimental results are in excellent agreement for particle volume fractions $\Phi < 1.5\%$, and we determine a maximum 6.5% error ($K_1 = 0.10$, $\Phi = 0.75\%$).

Additionally, we use the theoretical model, for which we document experimental validation in Fig. 3, to understand the effect of Φ, K_1, and K_2 on the local particle packing density after ultrasound DSA, covering the entire ultrasound DSA process envelope. Figure 4 shows the local packing density PD_{sim} at the location where particles assemble (node of the standing ultrasound wave) as a function of the particle volume fraction $0.75\% \leq \Phi \leq 27.50\%$, and as a function of the nondimensional particle size $0.05 \leq K_1 \leq 0.20$. We derive logistic curve best-fit equations to predict the particle packing density at the pattern features that result from ultrasound DSA (see Fig. 4) or, conversely, to determine the particle volume fraction Φ required to obtain a specific particle packing density. From Fig. 4, we observe that the particle packing density increases with increasing particle volume fraction Φ and with decreasing K_1, similar to the results of Fig. 3. However, we observe that the local particle packing density at the node of the standing ultrasound wave converges to 45%, independent of K_1, which is close to the maximum random particle packing density of spheres in 3D. Finally, we note that Fig. 4 includes parameter values that extrapolate beyond the parameter ranges used in the experimental validation and, thus, must be interpreted with caution.

Figure 5 shows the local packing density PD_{sim} at the location where particles assemble (node of the standing ultrasound wave) for $K_1 = 0.10$ as a function of the particle volume fraction Φ and the nondimensional viscosity of the mixture of particles and photopolymer $3.3 \times 10^3 \leq K_2 \leq 9.8 \times 10^3$. We derive logistic curve best-fit equations to predict the particle packing density at the pattern features that result from ultrasound DSA or, conversely, to determine the particle volume fraction Φ required to obtain a specific particle packing density. From Fig. 5, we observe that the particle packing density increases with increasing particle volume fraction Φ, independent of K_2, similar to the results of Figs. 3 and 4. We also observe that the local particle packing density at the node of the standing ultrasound wave converges to 45%, independent of K_2, which is close to the maximum random particle packing density of spheres in 3D. Thus, K_2 does not affect the local particle packing density; it only affects the speed by which particles assemble at the nodes. We account for the effect of medium viscosity on the attenuation of the incident wave, dipole scattering, and the amplitude of the acoustic radiation potential. However, the medium viscosity can also induce nonlinear phenomena such as streaming at the reservoir walls and even microstreaming around particles [67,68]. These phenomena can affect the local packing density for particle volume fractions $\Phi > 1.5\%$.

$$PD_{sim} = 26.20/(0.42 + \exp(-0.56\Phi)) - 18.45$$
$$PD_{sim} = 52.93/(0.70 + \exp(-0.29\Phi)) - 31.21$$
$$PD_{sim} = 25.12/(0.40 + \exp(-0.24\Phi)) - 17.97$$
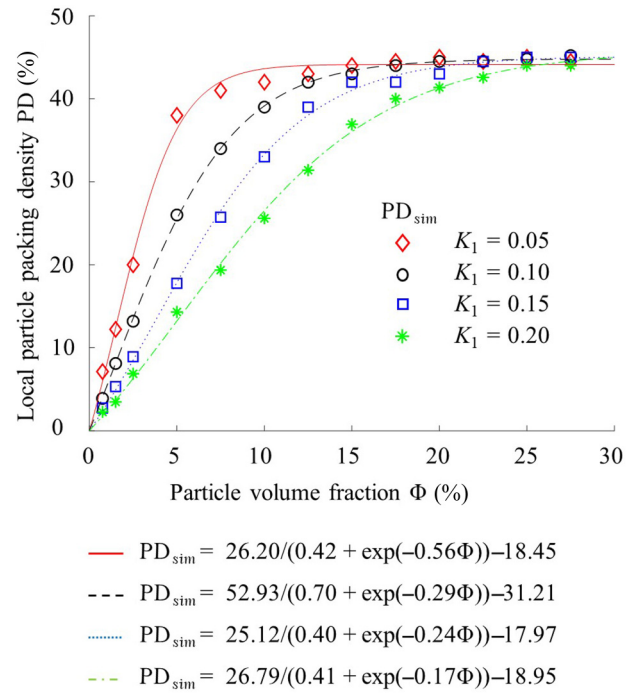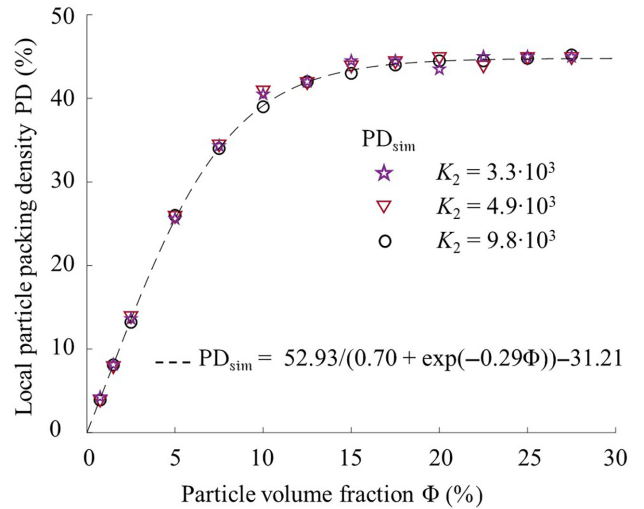$$PD_{sim} = 26.79/(0.41 + \exp(-0.17\Phi)) - 18.95$$

FIG. 4.   Local packing density within the pattern features that result from ultrasound DSA (node of the standing ultrasound wave) as a function of the particle volume fraction Φ, for $0.05 \leq K_1 \leq 0.20$.

Figure 6 shows the local particle packing density PD_{sim} at the location where particles assemble (node of the standing ultrasound wave) for $K_1 = 0.10$ and $K_2 = 3.3 \times 10^3$ as a function of the particle volume fraction Φ with logistic curve best-fit equations, when considering single

FIG. 5.   Local packing density within the pattern features that result from ultrasound DSA (node of the standing ultrasound wave) as a function of the particle volume fraction Φ, for $3.3 \times 10^3 \leq K_2 \leq 9.8 \times 10^3$, and with $K_1 = 0.10$.
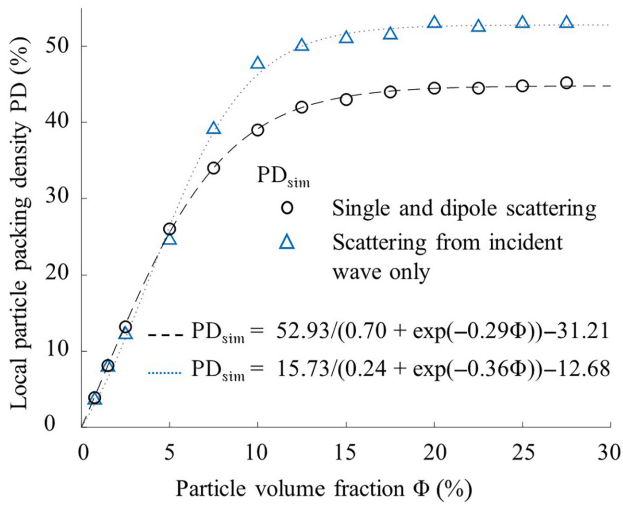
FIG. 6. Local particle packing density within the pattern features that result from ultrasound DSA (node of the standing ultrasound wave) as a function of the particle volume fraction Φ with $K_1 = 0.10$ and $K_2 = 3.3 \times 10^3$, accounting for single monopole and dipole scattering (black circles) and when considering only scattering resulting from the incident wave (blue triangles).

monopole and dipole scattering (black circle) and when considering single monopole and dipole scattering (black circle) and when only considering scattering resulting from the incident wave (blue triangle). From Fig. 6, we observe that the local particle packing density at the node of the standing ultrasound wave converges to 45% and 53% when we consider and neglect single monopole and dipole scattering, respectively. We attribute this difference to a repulsive acoustic particle interaction force that results from scattering, which agrees with results from Pavlic *et al.* [68], who report a repulsive acoustic interaction force in the direction of wave propagation between two copper microparticles ($a = 5$ μm, and $ka = 0.01$), and Silva and Bruus [13]. We also point out that based on modeling the interactions between particles using monopole and dipole scattering, one can also derive the interaction force between spherical particles [13].

IV. CONCLUSIONS

This work presents a 3D theoretical model of ultrasound DSA in a viscous medium with multiple particles, which allows simulating the locations of spherical particles in an ultrasound wave field as a function of time, and quantifying the local packing density at locations where particles assemble. Based on the results of the experiments and simulations, we conclude the following.

1. The local particle packing density at the pattern features that result from ultrasound DSA depends on the particle volume fraction and particle size, because they determine the number of particles that assemble in one location, and how they pack together.

2. The viscosity of the medium in which we organize the particles does not affect the local particle packing density resulting from ultrasound DSA, but it determines the time particles required to assemble in specific pattern because increasing viscosity increases the drag force acting on the particles.

3. The maximum achievable local particle packing density is 45%, independent of particle size and medium viscosity. However, the volume fraction required to achieve the maximum particle packing density decreases with decreasing particle size.

We note that while we provide experimental validation of the model for particle volume fractions $\Phi < 1.5\%$, our simulation results extrapolate beyond $\Phi = 1.5\%$ and, thus, results must be interpreted with caution. The results of this work enable predicting the volume fraction of particles required to obtain a specific local particle packing density at the specific pattern features that result from ultrasound DSA and, thus, contribute to the physical understanding of this process, which is useful in the context of manufacturing engineered polymer matrix composite materials with ultrasound DSA and VP. Specifically, this work has implications for fabricating engineered composite materials with a high or a specific local particle packing density to tailor the properties of the composite material.

ACKNOWLEDGMENTS

CONFLICT OF INTERESTS

The authors declare no competing interests.

[1] J. Greenhall, F. Guevara Vasquez, and B. Raeymaekers, Ultrasound directed self-assembly of user-specified patterns of nanoparticles dispersed in a fluid medium, Appl. Phys. Lett. **108**, 103103 (2016).

[2] J. Greenhall, F. Guevara Vasquez, and B. Raeymaekers, Continuous and unconstrained manipulation of microparticles using phase-control of bulk acoustic waves, Appl. Phys. Lett. **103**, 074103 (2013).

[3] L. V. King, On the acoustic radiation pressure on spheres, Proc. R. Soc. London, Ser. A **147**, 212 (1934).

[4] K. Yosioka and Y. Kawasima, Acoustic radiation pressure on a compressible sphere, Acta Acust. Acust. **5**, 167 (1955).

[5] L. P. Gor'kov, On the forces acting on a small particle in an acoustical field in an ideal fluid, Sov. Phys. Dokl. **6**, 773 (1962).

[6] M. Settnes and H. Bruus, Forces acting on a small particle in an acoustical field in a viscous fluid, Phys. Rev. E: Stat., Nonlinear, Soft Matter Phys. **85**, 1 (2012).

[7] S. Noparast, F. Guevara Vasquez, and B. Raeymaekers, The effect of medium viscosity and particle volume fraction on ultrasound directed self-assembly of spherical microparticles, J. Appl. Phys. **131**, 0 (2022).

[8] V. F. K. Bjerknes, *Fields of Force: A Course of Lectures in Mathematical Physics Delivered December 1 to 23, 1905* (Columbia University Press, New York, 1906).

[9] T. F. W. Embleton, Mutual interaction between two spheres in a plane sound field, J. Acoust. Soc. Am. **34**, 1714 (1962).

[10] W. L. Nyborg, Theoretical criterion for acoustic aggregation, Ultrasound Med. Biol. **15**, 93 (1989).

[11] A. P. Zhuk, Hydrodynamic interaction of two spherical particles due to sound waves propagating perpendicularly to the center line, Sov. Appl. Mech. **21**, 307 (1985).

[12] S. Sepehrirahnama, F. S. Chau, and K.-M. Lim, Effects of viscosity and acoustic streaming on the interparticle radiation force between rigid spheres in a standing wave, Phys. Rev. E **93**, 023307 (2016).

[13] G. T. Silva and H. Bruus, Acoustic interaction forces between small particles in an ideal fluid, Phys. Rev. E **90**, 063007 (2014).

[14] S. Zhang, C. Qiu, M. Wang, M. Ke, and Z. Liu, Acoustically mediated long-range interaction among multiple spherical particles exposed to a plane standing wave, New J. Phys. **18**, 113034 (2016).

[15] Z. Guo, J. A. Wood, K. L. Huszarik, X. Yan, and A. Docoslis, AC electric field-induced alignment and long-range assembly of multi-wall carbon nanotubes inside aqueous media, J. Nanosci. Nanotechnol. **7**, 4322 (2007).

[16] Y. Yang, Z. Chen, X. Song, Z. Zhang, J. Zhang, K. K. Shung, Q. Zhou, and Y. Chen, Biomimetic anisotropic reinforcement architectures by electrically assisted nanocomposite 3D printing, Adv. Mater. **29**, 1 (2017).

[17] J. H. E. Promislow and A. P. Gast, Magnetorheological fluid structure in a pulsed magnetic field, Langmuir **12**, 4095 (1996).

[18] J. J. Martin, B. E. Fiore, and R. M. Erb, Designing bioinspired composite reinforcement architectures via 3D magnetic printing, Nat. Commun. **6**, 1 (2015).

[19] X. Chen and R. E. Apfel, Radiation force on a spherical object in an axisymmetric wave field and its application to the calibration of high-frequency transducers, J. Acoust. Soc. Am. **99**, 713 (1996).

[20] L. E. Kinsler, A. R. Frey, A. B. Coppens, and J. V. Sanders, *Fundamental of Acoustic* (Wiley, New York, 2000), 4th ed.

[21] X. Ding, S. C. S. Lin, B. Kiraly, H. Yue, S. Li, I. K. Chiang, J. Shi, S. J. Benkovic, and T. J. Huang, On-chip manipulation of single microparticles, cells, and organisms using surface acoustic waves, Proc. Natl. Acad. Sci. U. S. A. **109**, 11105 (2012).

[22] R. Hirayama, D. Martinez Plasencia, N. Masuda, and S. Subramanian, A volumetric display for visual, tactile and audio presentation using acoustic trapping, Nature **575**, 320 (2019).

[23] A. Haake, A. Neild, D.-H. Kim, J.-E. Ihm, Y. Sun, J. Dual, and B.-K. Ju, Manipulation of cells using an ultrasonic pressure field, Ultrasound Med. Biol. **31**, 857 (2005).

[24] M. Evander and J. Nilsson, Acoustofluidics 20: Applications in acoustic trapping, Lab Chip **12**, 4667 (2012).

[25] Y. Yamakoshi, Y. Koitabashi, N. Nakajima, and T. Mlwa, Yeast cell trapping in ultrasonic wave field using ultrasonic contrast agent, Jpn. J. Appl. Phys., Part 1 **45**, 4712 (2006).

[26] B. Jung, K. Fisher, K. D. Ness, K. A. Rose, and R. P. Mariella, Acoustic particle filter with adjustable effective pore size for automated sample preparation, Anal. Chem. **80**, 8447 (2008).

[27] T. A. Ogden, M. Prisbrey, I. Nelson, B. Raeymaekers, and S. E. Naleway, Ultrasound freeze casting: fabricating bioinspired porous scaffolds through combining freeze casting and ultrasound directed self-assembly, Mater. Des. **164**, 107561 (2019).

[28] M. Mroz, J. L. Rosenberg, C. Acevedo, J. J. Kruzic, B. Raeymaekers, and S. E. Naleway, ultrasound freeze-casting of a biomimetic layered microstructure in epoxy-ceramic composite materials to increase strength and hardness, Materialia **12**, 100754 (2020).

[29] E. V. Skorb, H. Möhwald, T. Irrgang, A. Fery, and D. V. Andreeva, Ultrasound-assisted design of metal nanocomposites, Chem. Commun. **46**, 7897 (2010).

[30] M. D. Haslam and B. Raeymaekers, Aligning carbon nanotubes using bulk acoustic waves to reinforce polymer composites, Composites, Part B **60**, 91 (2014).

[31] J. Greenhall, L. Homel, and B. Raeymaekers, Ultrasound directed self-assembly processing of nanocomposite materials with ultra-high carbon nanotube weight fraction, J. Compos. Mater. **53**, 1329 (2019).

[32] A. K.-T. Lau and D. Hui, The revolutionary creation of new advanced materials—carbon nanotube composites, Composites, Part B **33**, 263 (2002).

[33] D. S. Melchert, R. R. Collino, T. R. Ray, N. D. Dolinski, L. Friedrich, M. R. Begley, and D. S. Gianola, Flexible conductive composites with programmed electrical anisotropy using acoustophoresis, Adv. Mater. Technol. **4**, 1900586 (2019).

[34] K. Niendorf and B. Raeymaekers, Combining ultrasound directed self-assembly and stereolithography to fabricate engineered polymer matrix composite materials with anisotropic electrical conductivity, Composites, Part B **223**, 109096 (2021).

[35] K. Niendorf and B. Raeymaekers, Using supervised machine learning methods to predict microfiber alignment and electrical conductivity of polymer matrix composite materials fabricated with ultrasound directed self-assembly and stereolithography, Comput. Mater. Sci. **206**, 111233 (2022).

[36] T. Mulholland, S. Goris, J. Boxleitner, T. A. Osswald, and N. Rudolph, Fiber orientation effects in fused filament fabrication of air-cooled heat exchangers, JOM **70**, 298 (2018).

[37] K. J. White, I. Stobie, W. Oberle, G. Katulka, and S. Driesen, Combustion control requirements in high loading density, solid propellant ETC gun firings, IEEE Trans. Magn. **33**, 350 (1997).

[38] Z. Xiao, S. Ying, and F. Xu, Deconsolidation and combustion performance of thermally consolidated propellants

deterred by multi-layers coating, Def. Technol. **10,** 101 (2014).

[39] W. Yang, R. Hu, L. Zheng, G. Yan, and W. Yan, Fabrication and investigation of 3D-printed gun propellants, Mater. Des. **192,** 108761 (2020).

[40] J. Greenhall and B. Raeymaekers, 3D printing macroscale engineered materials using ultrasound directed self-assembly and stereolithography, Adv. Mater. Technol. **2,** 1700122 (2017).

[41] M.-S. Scholz, B. W. Drinkwater, and R. S. Trask, Ultrasonic assembly of anisotropic short fibre reinforced composites, Ultrasonics **54,** 1015 (2014).

[42] R. R. Collino, T. R. Ray, R. C. Fleming, C. H. Sasaki, H. Haj-Hariri, and M. R. Begley, Acoustic field controlled patterning and assembly of anisotropic particles, Extreme Mech. Lett. **5,** 37 (2015).

[43] L. Friedrich, R. Collino, T. Ray, and M. Begley, Acoustic control of microstructures during direct ink writing of two-phase materials, Sens. Actuators, A **268,** 213 (2017).

[44] P. Wadsworth, I. Nelson, D. L. Porter, B. Raeymaekers, and S. E. Naleway, Manufacturing bioinspired flexible materials using ultrasound directed self-assembly and 3D printing, Mater. Des. **185,** 108243 (2020).

[45] K. Niendorf and B. Raeymaekers, Additive manufacturing of polymer matrix composite materials with aligned or organized filler material: A review, Adv. Eng. Mater. **2001002,** 1 (2021).

[46] D. E. Yunus, S. Sohrabi, R. He, W. Shi, and Y. Liu, Acoustic patterning for 3D embedded electrically conductive wire in stereolithography, J. Micromech. Microeng. **27,** 045016 (2017).

[47] T. M. Llewellyn-Jones, B. W. Drinkwater, and R. S. Trask, 3D printed components with ultrasonically arranged microscale structure, Smart Mater. Struct. **25,** 02LT01 (2016).

[48] K. Niendorf and B. Raeymaekers, Quantifying macro- and microscale alignment of carbon microfibers in polymer-matrix composite materials fabricated using ultrasound directed self-assembly and 3D-printing, Composites, Part A **129,** 105713 (2020).

[49] L. Lu, Z. Zhang, J. Xu, and Y. Pan, 3D-printed polymer composites with acoustically assembled multidimensional filler networks for accelerated heat dissipation, Composites, Part B **174,** 106991 (2019).

[50] C. V. Driel, M. Straathof, and J. V. Lingen, in 30th International Symposium on Ballistics (2017).

[51] H. Y. Sohn and C. Moreland, The effect of particle size distribution on packing density, Can. J. Chem. Eng. **46,** 162 (1968).

[52] J. H. Conway and N. J. A. Sloane, *Sphere Packings, Lattices and Groups* (Springer New York, New York, NY, 1999), Vol. 290.

[53] G. D. Scott and D. M. Kilgour, The density of random close packing of spheres, J. Phys. D: Appl. Phys. **2,** 863 (1969).

[54] C. Song, P. Wang, and H. A. Makse, A phase diagram for jammed matter, Nature **453,** 629 (2008).

[55] A. E. R. Westman and H. R. Hugill, The packing of particles, J. Am. Ceram. Soc. **13,** 767 (1930).

[56] K. W. Chan and A. K. H. Kwan, Evaluation of particle packing models by comparing with published test results, Particuology **16,** 108 (2014).

[57] S. John Milne, M. Patel, and E. Dickinson, Experimental studies of particle packing and sintering behaviour of monosize and bimodal spherical silica powders, J. Eur. Ceram. Soc. **11,** 1 (1993).

[58] R. S. Farr and R. D. Groot, Close packing density of polydisperse hard spheres, J. Chem. Phys. **131,** 244104 (2009).

[59] J. Zheng, W. B. Carlson, and J. S. Reed, The packing density of binary powder mixtures, J. Eur. Ceram. Soc. **15,** 479 (1995).

[60] F. Zok, F. F. Lange, and J. R. Porter, Packing density of composite powder mixtures, J. Am. Ceram. Soc. **74,** 1880 (1991).

[61] DLMF: §10.49 Explicit Formulas âĂč Spherical Bessel Functions âĂč Chapter 10 Bessel Functions, https://dlmf.nist.gov/10.49

[62] A. A. Doinikov, Acoustic radiation force on a spherical particle in a viscous heat-conducting fluid. ii. force on a rigid sphere, J. Acoust. Soc. Am. **101,** 722 (1997).

[63] A. R. Khan and J. F. Richardson, The resistance to motion of a solid sphere in a fluid, Chem. Eng. Commun. **62,** 135 (1987).

[64] X. Wang, S. Ramírez-Hinestrosa, J. Dobnikar, and D. Frenkel, The Lennard-Jones potential: When (not) to use it, Phys. Chem. Chem. Phys. **22,** 10624 (2020).

[65] W. M. Haynes, D. R. Lide, and T. J. Bruno, *CRC Handbook of Chemistry and Physics* (CRC Press, Boca Raton, 2014), 95th ed.

[66] E. E. Underwood, Stereology, or the quantitative evaluation of microstructures, J. Microsc. **89,** 161 (1969).

[67] N. St. Clair, D. Davenport, A. D. Kim, and D. Kleckner, Dynamics of acoustically bound particles, Phys. Rev. Res. **5,** 013051 (2023).

[68] A. Pavlic, L. Ermanni, and J. Dual, Interparticle attraction along the direction of the pressure gradient in an acoustic standing wave, Phys. Rev. E **105,** L053101 (2022).